Lab on a Chip

Droplet Delivery and Nebulization System Using Surface Acoustic Wave for Mass Spectrometry

Journal:	*Lab on a Chip*
Manuscript ID	LC-ART-05-2020-000495.R1
Article Type:	Paper
Date Submitted by the Author:	12-Jul-2020
Complete List of Authors:	Sun, Di; University of Washington, Electrical Engineering Bohringer, Karl; University of Washington, Electrical Engineering Sorensen, Matthew; Deurion LLC Nilsson, Erik; Deurion LLC Edgar, Scott; University of Washington, Department of Medicinal Chemistry Goodlett, David; University of Maryland, School of Dentistry

ARTICLE

DROPLET DELIVERY AND NEBULIZATION SYSTEM USING SURFACE ACOUSTIC WAVE FOR MASS SPECTROMETRY

Received 00th January 20xx,
Accepted 00th January 20xx

DOI: 10.1039/x0xx00000x

Di Sun,[ab] Karl F. Böhringer,[*ab] Matthew Sorensen,[c] Erik Nilsson,[c] J. Scott Edgar,[d] and David R. Goodlett[ef]

We present a piezoelectric transducer for standing wave surface acoustic wave nebulization (SW-SAWN). The transducer nebulizes nonvolatile analytes present in bulk fluid into ambient air after which aerosolized drops are sampled by mass spectrometry (MS) for detection. Furthermore, we report for the first time integration of anisotropic ratchet conveyors (ARCs) on the SAWN transducer surfaces to automate the sample preparation and droplet delivery process. The ARCs employ micro-sized hydrophilic patterns on hydrophobic Cytop coatings. Moving, positioning, merging, and mixing of droplets at a designated nebulization location are demonstrated. To create the ARCs, we adopt Parylene C as a stencil mask so that the hydrophobicity of the Cytop does not degrade during the microfabrication process. MS measurements with the SAWN chip are performed under different input frequencies. The SAWN transducer can provide a controllable nebulization rate by varying the input nebulization frequency while maintaining a reasonable signal to noise ratio for MS detection.

Introduction

Within the field of proteomics, there is a general interest in developing platforms that simplify the sample preparation process, to reduce the volume of fluid analytes used to prepare peptides and proteins for analysis by available mass spectrometry (MS) as well as to eliminate sample contamination. It is equally important that these platforms are compatible with the current commercially available MS due to the widespread use of MS in proteomics. However, integrating both fluid analyte manipulation and aerosolization capabilities for MS remains a challenge.

Digital microfluidics enables liquid manipulation in discrete droplet formats and provides a lab-on-a-chip (LOAC) platform. The LOAC platform provides flexible and complex droplet manipulations, including creating, cutting, moving, merging and mixing droplets[1-4]. There are multiple techniques available for digital microfluidics including heat,[5-7] optics,[8, 9] magnetic fields,[10] mechanical vibrations,[11, 12] electrowetting-on-dielectric (EWOD),[13-15] liquid dielectrophoresis (L-DEP)[16] and acoustic fields.[4, 17] In order to interface LOAC platforms with MS, analyte ionization techniques are required. Two popular approaches, namely electrospray ionization (ESI)[18] and matrix assisted laser desorption ionization (MALDI),[19, 20] are widely used. The ESI process uses a high potential electrical capillary that ejects a stream of positively charged drops. During the path of flight, the charged droplets break into charged ions due to solvent evaporation and Coulombic fission. Notably, ESI effectively handles a large detectable mass range[21] with impressive sensitivity. To produce ions by MALDI, typically a specific matrix solution is first mixed with the sample and allowed to co-crystallize on a metal plate. The pulsed laser ablation on the metal surface creates ionized analyte molecules for MS analysis. MALDI provides a rapid, sensitive, and low-cost method and can examine multiple samples at the same time. Integrated digital microfluidic platforms and aerosolization techniques have also been demonstrated with parallel sample processing capability[22] and improved detection signal intensity.[23]

However, nonideal scenarios may occur in both aerosolization methods because of the nature of the analyte or the solvent. For ESI, a high voltage potential must be applied to the liquid analytes during the ionization process. The accessories in the ESI system, such as channels, nozzles, and capillaries, are easily fouled by the liquid analytes. For MALDI, matrix ions can interfere with low mass-to-charge ratio (m/z) analyte ions. In this paper, we present development of an aerosolization interface by adopting surface acoustic wave nebulization (SAWN). SAW technology has been widely adopted in various commercial devices such as tactile displays,[24, 25] radio frequency filters,[26, 27] microfluidic

[a] Department of Electrical and Computer Engineering, University of Washington, Seattle, WA 98195, USA. Email: karlb@uw.edu; Tel: +1-206-221-5177.
[b] Institute for Nano-Engineered Systems, University of Washington, Seattle, WA 98195, USA.
[c] Deurion LLC, Seattle, WA 98103, USA.
[d] Department of Medicinal Chemistry, University of Washington, Seattle, WA 98195, USA.
[e] School of Dentistry, University of Maryland, Baltimore, MD 21201, USA.
[f] International Centre for Cancer Vaccine Science, University of Gdansk, Gdansk, Poland, EU.

systems,[28-30] chemical sensors[31] and optomechanical systems.[32, 33] The SAWN platform creates ions from bulk liquid analytes directly in an ambient environment at atmospheric pressure. SAWN can operate in either a continuous mode or intermittent mode. Typically, the vibration frequency is high (10 MHz) but the excitation power is relatively low.[34] SAWN does not require high voltage and as a result provides advantages for labile molecule analysis.[35, 36] Moreover, there is no interference with low *m/z* analyte ions on the SAWN platform which unlike MALDI uses no matrix that can interfere.[37]

In general, there are challenges to 1) automatically deliver a droplet on the SAWN platform for mechanical clearance from stationary dispensing; 2) make nebulization droplet location consistent for each entire droplet and from droplet to droplet; and 3) seamlessly nebulize the analytes in solvent on chip into the gaseous phase. Integration of droplet manipulation functions to precisely deliver, position, mix and merge analytes are desirable for a potentially automated SAWN platform with mass spectrometer.[38] For example, to better control the nebulization location, superstrate designs with a periodic phononic crystal structure have been created by etching an array of holes into the Si substrate. The phononic crystal structure enabled a strong confinement of the acoustic field and presented a disposable fluidic platform[39, 40] that reduced the high cost of piezoelectric substrate materials.

Here, we present use of a droplet directional manipulation approach to combine anisotropic ratchet conveyors (ARC)[11, 41] with the SAWN platform. ARCs utilize hydrophilic patterns on a hydrophobic background to control the droplet transport by imbalanced hysteresis force when the droplet contact lines advance and recede on the patterned surfaces. The technology has the ability to make a droplet follow complex patterns, e.g. a zig-zag path that cleans surface contaminants.[42, 43] By creating ARC patterns on a SAWN surface, we can control the directional movement of the droplet and confine the droplet position during the nebulization process. Compared with the superstrate method, the ARC pattern is created solely from polymeric thin films without the need to etch deep Si structures. Additionally, while not shown here samples could be mixed on chip allowing some basic chemistry (e.g. hydrogen-deuterium exchange[44]) to take place prior to nebulization. Mass spectrometry results using a SAWN source are presented under different input resonance frequencies, which demonstrates a controllable nebulization rate by altering the input frequencies.

Materials and methods

Device design

The design of the standing wave SAWN device with ARC patterning is shown in Fig. 1. The total width of the active interdigitated electrodes (IDE) region (W_{IDE}) is 10 mm. Considering the propagation speed of SAW is 3960 m/s at the excitation frequency of 9.56 MHz, the linewidth (I_E) and gap between the adjacent edges (I_G) of the metal electrodes are designed to be λ/4 = 103.6 μm. To generate and optimize standing waves, the distance between the two excitation electrodes (L) needs to be designed as (n+0.5)λ by superposition of progressive waves generated by the top and bottom IDEs,[45] where n is an integer and λ is the wavelength. In our design, λ = 414.4 μm and n = 15, giving a distance of L = 6.2 mm.[35, 37, 46] The distance between the excitation electrode and the reflection electrode (d_R) is designed to be λ/8 = 51.8 μm. The number of excitation electrode pairs (N_O) is 20 and the number of the reflector electrodes (N_R) is 32. There are two input channels on the SAWN chip so that the SAWN chip can be operated with both progressive mode and standing wave mode. The input power can be adjusted accordingly through the commercial driving power supply. To verify our design, we performed an S11 measurement with a vector network analyzer (8753D, Agilent Inc.). Shown in Fig. 1(d), the dips along the S11 measurement curve present the surface acoustic wave resonance frequencies. We also performed 2D finite element simulations to estimate the SAW modes. The simulation model consisted of $LiNbO_3$ substrates with periodic structural boundary conditions on both sides of the simulation cell. The height of the simulation cell was designed large enough to prevent any SAW reflection by the bottom boundary of the simulation cell. The Fig. 1(d) inserts demonstrate the simulation results of two lowest-order SAW modes. The detailed material matrix used for the simulation model is shown in the Supplementary S1. The simulation result of resonance frequency matched well with the S11 measurement result.

Fig. 1(b) and 1(c) show two typical designs of the ARC patterns on the SAWN chip surface. The droplet can be transported in parallel with the SAW transport direction or at an angle. In Fig. 1(c), the two side ARC tracks have a 45° angle compared to the center ARC track. Hydrophilic arc-shaped rungs (trimethylsilanol, TMS) were patterned on a hydrophobic Cytop coating. As for the ARC patterns, the rung period pitch (P) is 50 μm, the hydrophilic line width (w) is 10 μm, and the ARC track width (W_{ARC}) is 500 μm. We designed a hydrophilic circle at the center of the chip for droplet merging or nebulization operation. The diameter of the central hydrophilic circle (D) is 1000 μm.

A droplet on the SAW platform with hydrophobic coating can go through periodic distortion due to SAW acoustic pressure.[47] As modulated, the water droplet wets the ratchet patterns along the rungs, creating an air-water-solid three-phase contact line (TPL) along its outer edge. We denoted the portion of the water droplet edge that aligns with the rung curvature, which has a mostly continuous TPL, as the leading edge of the droplet, while the other portion, which has only intermittent TPLs across different rungs, is called the trailing edge of the droplet. The leading edge of the droplet provides a higher pinning force than the trailing edge as the water droplet expands and recesses on the hydrophobic-hydrophilic boundary of the ARC patterns. This asymmetry in pinning forces causes water droplets to move toward the direction of the rung curvature.[48]

Fabrication process

To fabricate the SAWN device, we used a 3-inch single side polished 128° YX-cut $LiNbO_3$ substrate with a thickness of 500 μm. The wafer was first cleaned to remove any contaminants or dust that could affect the spun layer of the resist. IDEs were patterned on the polished side by a standard lithography process. Cr and Au layer electrodes were deposited via an e-beam evaporator and the substrate was soaked in acetone for photoresist lift-off. The wafer was cut into individual SAWN chips before further testing.

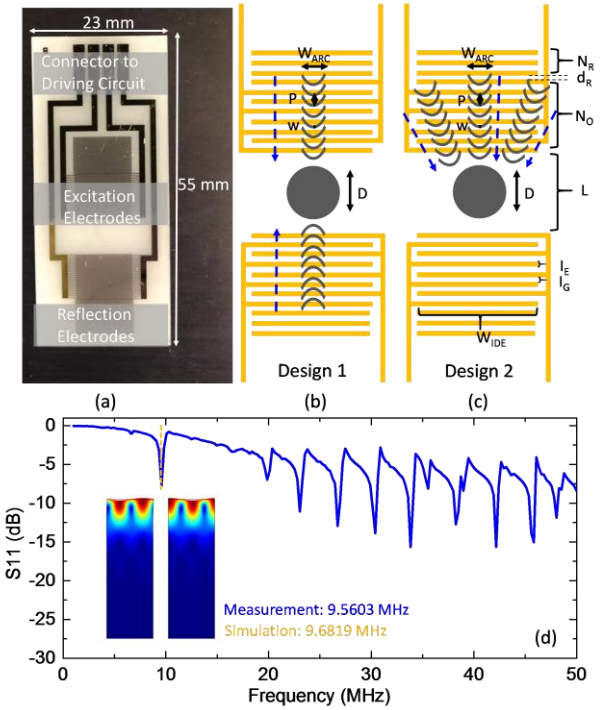

Fig. 1 SAWN chip design with ARC and frequency measurements. (a) Top view of the SAWN chip after dicing. (b) and (c) SAWN platform setup with ARC. Two designs of the ARC patterns for droplet movement control. Dotted blue arrows indicate the droplet movement direction. The grey arc-shaped rungs and center circle patterns are hydrophilic regions, treated with TMS. The other regions of the SAWN chip are covered with Cytop. (d) The S11 measurement result of the SAWN chip. The scanning start frequency is 1 MHz and the end frequency is 50 MHz. The inserts show the simulated transverse and longitudinal SAW modes at the lowest order resonance frequency, corresponding to the frequency at the ochre dotted line from the S11 curve. The general trend for S11 value decreases at higher frequencies, which could come from the resistive energy loss at the electrical connection.

To create Cytop-TMS patterns on the SAWN surface, we utilized Parylene C as a stencil mask.[48] Direct spin coating of photoresist could not form a uniform layer on top of the hydrophobic Cytop surface. Diluted Cytop (Asashi Glass Co. Ltd) solution (Cytop : CT solv180 = 1:3) was spin-coated and baked at 180 °C for 1 hour with a final thickness of ~70 nm. Then a 2.5 μm Parylene C film was evaporated on the Cytop using a commercial parylene coater (PDS 2010, Specialty Coating Systems, Inc.) under vacuum. 6 μm photoresist (AZ9260, MicroChemicals GmbH) was spin-coated on Parylene C and directly exposed with a Heidelberg-MicroPG-101 mask writer (Heidelberg Instruments Mikrotechnik GmbH). The photoresist was developed with AZ400K photoresist developer (AZ400K : DI water = 1:4) for 3 min. Then the exposed Parylene C regions were etched with O_2 plasma using a reactive ion etching process (Vision 320 RIE Mark II, Advanced Vacuum, Inc.). Both the patterned Parylene C and the Cytop underneath were etched with this process. The Parylene C mask was carefully peeled off from the substrate with tweezers. A spin-on TMS layer (MP-P20, ShinEtsu MicroSi, Inc.) was deposited on the Cytop openings followed by baking on a hotplate for 2 min. The fabrication flow schematic is shown in Supplementary S2.

Droplet manipulation test setup

Both progressive wave surface acoustic wave nebulization (PW-SAWN) and standing wave surface acoustic wave nebulization (SW-SAWN) modes can be generated by a commercial power supply (Deurion LLC), outputting a SAW wave at 9.56 MHz. A water droplet was pipetted, and the droplet silhouette was monitored by a high-speed camera (FASTCAM Mini UX100, Photron Inc.) with a sampling rate of 1000 fps. The droplet position and contact angle change with time were analyzed with our MATLAB/Python custom code. The droplet static contact angle was analyzed with ImageJ software. The droplet sliding angle was characterized by a custom-made tilting stage. The inclination angle was measured with a triple-axis accelerometer (MMA8451, Adafruit, Inc.). The size of the tiny drops after nebulization was measured by an aerodynamic particle sizer spectrometer (APS Model 3321, TSI Incorporated). The aerosol flow was set to 1 L/min and the sheath flow was 4 L/min. The measurement range of the aerodynamic particle sizer spectrometer was set from 0.5 to 10 μm.

Droplet nebulization test setup

The mass spectrometry (MS) experiments were performed on a SYNAPT G2-Si high definition mass spectrometer (Waters Corp.). The SW-SAWN mode chip was mounted on a custom-made chip holder and placed close to the G2 MS inlet. The droplets on the SAWN chip surface containing dissolved analytes were nebulized into a plume of aerosolized drops as the SAW reached the liquid. The drops were sampled by SYNAPT's atmospheric pressure ionization (API) interface. Frequencies higher than the fundamental frequency were tested to nebulize the droplets. The nebulization frequencies were first selected based on the S-parameter measurements by the vector network analyzer (8753D, Agilent Inc.). Then the analog signal generator (N5181a, Agilent Inc.) was connected to two broadband (2 MHz – 700 MHz) RF power amplifiers on each channel of the SAWN chip. The gain of the power amplifier was 35 dB and the input power from the analog signal generator was set as 0 dBm (1 mW).

We used MS standard Angiotensin II (ProteoMass, Sigma-Aldrich) dissolved in 0.1% acetic acid in water for the MS measurement. Different concentrations (1 μM and 100 nM) of the analyte solution were tested.

Results and discussion

Cytop patterning

The ARC tracks were successfully patterned on the Cytop coated $LiNbO_3$ substrate (Fig. 2 (a)) and IDE electrodes (Fig. 2 (b)). We characterized the Cytop surface properties by comparing the static contact angle (CA) and sliding angle (SA) of the as-deposited Cytop surface and the Cytop surface after patterning with Parylene C. 10 μL water droplets were used to characterize CA and 15 μL droplets were used for SA. Each analysis result was generated from three water droplets at different substrate locations. Shown in Fig. 2 (c), as evident from the results, Cytop maintained hydrophobic surface properties with high CA and low SA after peeling off the patterned Parylene C stencil mask.

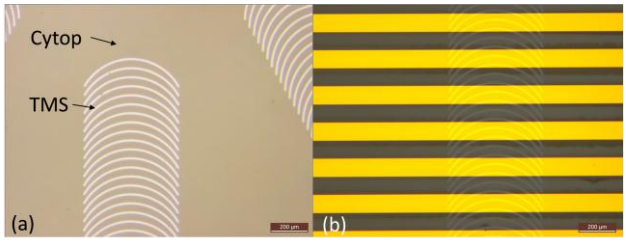

(c)

Parameter	Process	Average (°)	Std. (°)
Contact Angle	As deposited	113.3	0.5
	After parylene removal	109.7	0.9
Sliding Angle	As deposited	19.8	2.6
	After parylene removal	20.8	2.7

Fig. 2 Finished ARC patterns on top of the (a) $LiNbO_3$ substrate surface and (b) Cr/Au metal electrodes region. (c) Table comparing the Cytop surface properties as deposited and after peeling off Parylene C.

Droplet transport characterization

We operated the SAWN chip in standing wave mode for the droplet delivery and the nebulization characterizations. Compared with PW-SAWN, SW-SAWN provides a gain of 10^2-fold to 10^3-fold in ion intensity for peptides with smaller nebulized drop size distribution [35, 49]. When the SAW power was turned on, the droplet was first distorted by the acoustic pressure and elongated vertically. Then the droplet restored its shape and wetted the surface. The distortion and restoration of the droplet were periodic, monitored by a high-speed camera. The leading and trailing edge of the droplet then periodically wetted and dewetted along the ARC patterns to create an anisotropic pinning force. As shown in Fig. 3 (a), a

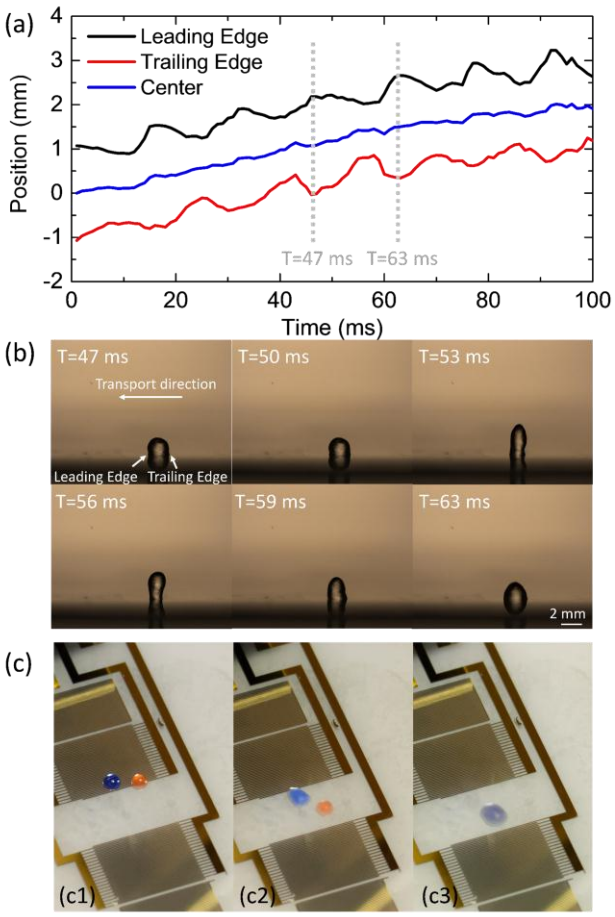

Fig. 3 Analysis of droplet movement on SAWN-ARC chips. (a) Droplet edge position change with time, modulated by the SAWN power. The average transport speed can be estimated from the center position change over 100 ms sampling time. (b) High-speed camera capture of droplet silhouettes (Movie S1). (c) Droplets moving and merging operation on SAWN platform with ARC tracks. (c1) Placement of colored droplets (blue and orange) on the two ARC tracks. (c2) Droplets moving along ARC actuated by SAW. (c3) Droplets stopping, merging and mixing at the central hydrophilic nebulization region.

3 μL droplet was transported at about 9 W input power with the standing wave mode at the SAWN frequency of 9.56 MHz. The input of the SW-SAW power was continuous as the droplet transported along the ARC patterned tracks. The leading edge expanded at 0.60 mm ± 0.09 mm and recessed at 0.26 mm ± 0.13 mm during each oscillation cycle, while the trailing edge expanded at 0.31 mm ± 0.11 mm and recessed at 0.65 mm ± 0.14 mm. The droplet transported at an average speed of 20 mm/s. The periodicity of the droplet behaviour was observed at ~16 ms (63 Hz) by analyzing the position change of the leading and trailing edge over time. The droplet ended up at the hydrophilic circle patterned on the center location of the SAWN chip even with continuous input of the SW-SAW power (Movie S1). The droplet would nebulize when the actuation power was increased. Droplet silhouettes during a single oscillation cycle are shown in Fig. 3 (b). Fig. 3 (c) demonstrate the droplet merging and mixing function on the ARC designs shown in Fig. 1 (c). The operation was performed in an open environment without enclosed channels or top covers and

without the need for complex control circuitry. One colored droplet (blue) was pipetted on the center ARC track and the other colored droplet (orange) was applied on one of the side track with 45° angle. The continuous SW-SAW (9.56 MHz at 9 W) modulated the two droplets to transport along their own ARC tracks at the same time. The droplets moved to the central hydrophilic circle regions, where they were mixed with high-frequency SAW vibrations. Creating ARC patterns and central hydrophilic circles helped to automatically reposition and hold the droplet on the SAWN chip. The mixing function can provide droplet manipulation possibilities to complete tasks like sample dilution or pH adjustment.

To more precisely describe the periodic oscillation of the droplet under the SAW field, we tracked the droplet width and height change with time. As shown in Fig. 4 (a), the droplet started as a semi-spherical shape on the SAWN chip surface (step I). It then started to elongate vertically (step II) and reached the maximum distortion in height (step III). Then the droplet recessed (step IV) and expanded slightly along the horizontal direction, wider than the original droplet width, before the droplet completely restored its initial hemispherical shape to complete the cyclical distortion (step I). We denoted the droplet initial width as w_{drop0} and the droplet initial height as h_{drop0}. The normalized droplet width and height changes with time compared to the initial value are shown in Fig. 4 (b). The cyclical distortion frequency was related to the droplet size, demonstrated in Fig. 4 (c). As the droplet volume decreased, the droplet cycled through the distortion phase and restoration phase faster. We believe that the periodic oscillation frequency of different droplet volumes was associated with the eigen mode of the droplet driven by the inertial-capillary forces[50]. The SAW acoustic pressure applied on the droplet free surface caused the droplet to distort vertically. The base of the droplet shrunk and thus the acoustic pressure decreased. The distorted droplet tended to restore its original shape to minimize surface energy under the influence of capillarity[51].

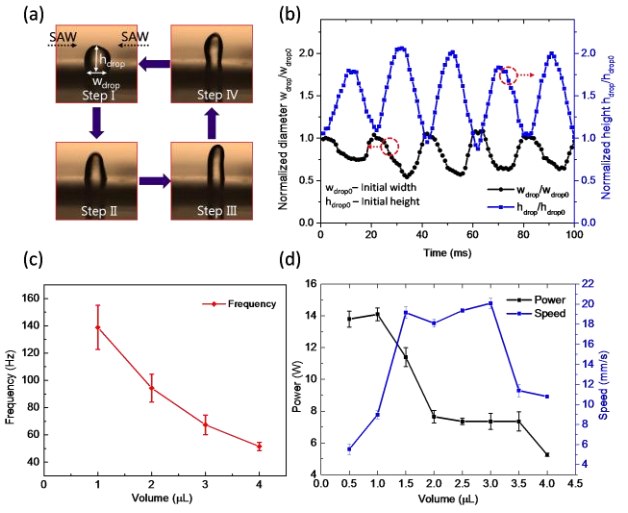

Fig. 4 Measurements of droplet parameters. (a) Steps of the periodical droplet distortion under SAW actuation. (b) Normalized droplet width and height change with time as the droplet moved on the ARC track. The droplet size in this plot was 3 μL. (c) Characterized periodical distortion frequencies for different volumes of the droplet. Data is shown ± one standard deviation for n = 3. (d) Minimum power required to transport the droplet sitting on the ARC track by SAW and the droplet transport speed with the same input SAWN power. The droplet volumes ranged from 0.5 to 4 μL. Data is shown ± one standard deviation for n = 3.

We tested the minimum required power to transport the droplet by slowly increasing the input power until droplet movement was observed and recorded the average droplet movement speed at this input power, shown in Fig. 4 (d). The minimum power required to initiate droplet movement decreased as the droplet size increased. All the droplets tested (0.5 – 4 μL) were able to overcome the surface friction or contact angle hysteresis and were transported by SAW within the available power supply rating. The droplet transport speed was characterized with the input power of 15 W. The droplet transport speed involves the modelling of its complex interactions with the periodic heterogeneous ARC patterns[52, 53]. The speed of the droplet is given by $v = n \times P \times f$, where n is the number of ARC rungs by which the droplet advances during each vibration cycle, P is the pitch between ARC rungs, and f is the vibration frequency. For small droplets, f is large but n is small, while for large droplets, f is small but n is high. There is a maximum speed that is determined by this trade-off between f and n.

Droplet nebulization

We conducted the SAWN chip nebulization tests without the ARC coatings. Fig. 5 (a) demonstrates a successful nebulization process as the SAWN chip converted the bulk water droplet on top to a plume of fine drops. When the SAW met a liquid medium along its path, the leakage of the SAW from the substrate into the droplet caused internal liquid streaming and free capillary waves on the droplet surface[54]. When the power was high enough, the capillary waves at the droplet surface caused droplet pinch-offs[55]. Thus, a mist of aerosolized droplets overcame the capillary adhesion and jetted. The height of the aerosolized droplets plume could grow higher than 30 cm, providing a wide operating range when interfacing with the MS inlet. Besides the fundamental resonance frequency, we also tested the SAWN chip to nebulize at higher harmonic frequencies. The tested frequencies were picked from the S11 measurement results (shown in Fig. 1(d)), where a dip in the S11 curve demonstrated a strong coupling between the input AC voltage and mechanical SAW propagation. The nebulization capabilities at the fundamental resonance frequency and the higher-order resonance frequencies are shown in Fig. 5(b). It is interesting to note that the droplet cannot be nebulized or that it had an extremely weak nebulization process at the harmonics of the fundamental resonance frequency (19.8944 MHz and 30.4147 MHz). At higher frequencies (>38.2 MHz), the droplet could not be nebulized even though there was a strong dip in signal from the S11 curve, which could have been caused by the phase mismatch and the energy loss at the connectors.

We further characterized the nebulization time under ambient air environment (27 °C and 40% RH). For each of the

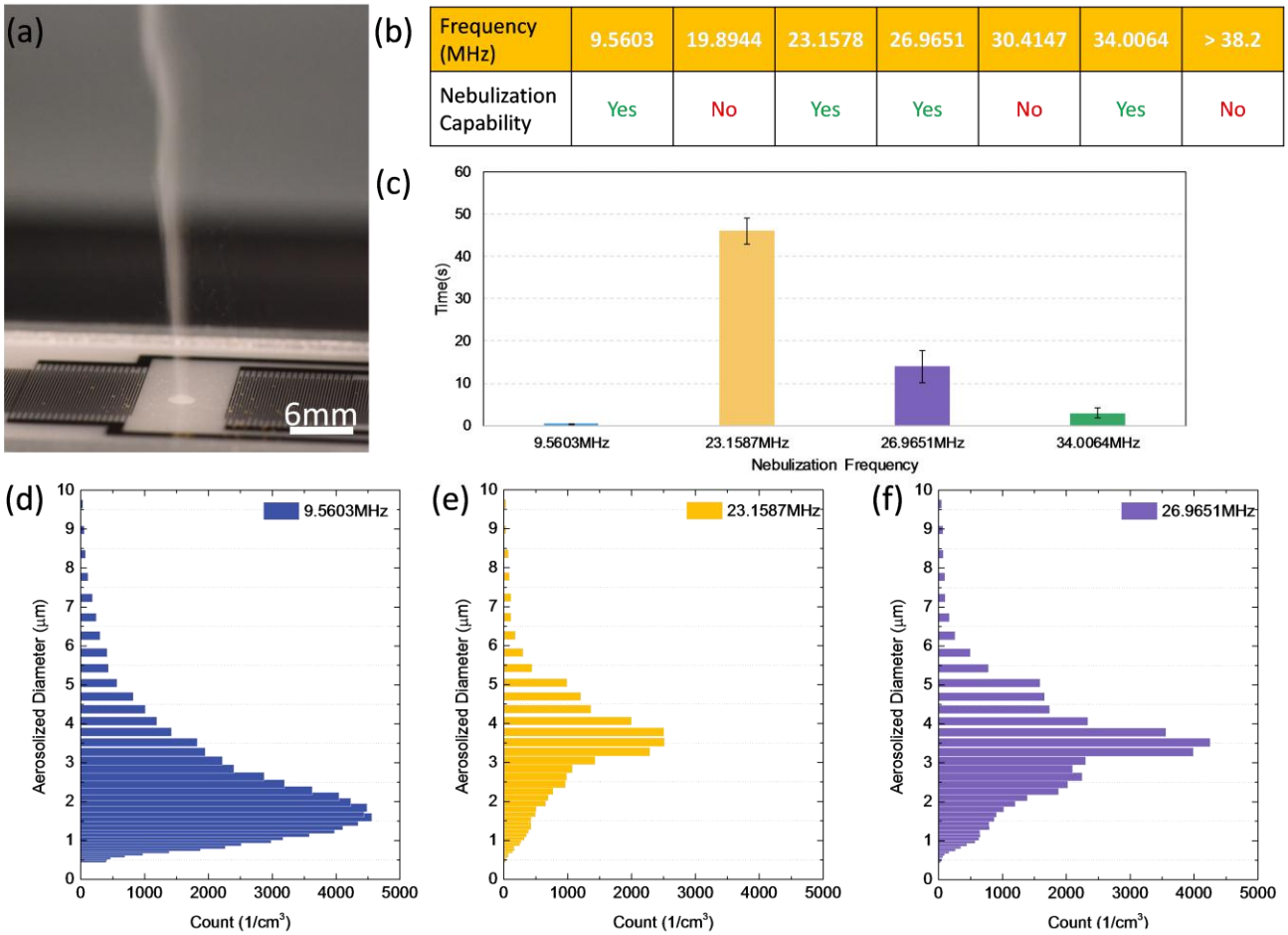

Frequency (MHz)	9.5603	19.8944	23.1578	26.9651	30.4147	34.0064	> 38.2
Nebulization Capability	Yes	No	Yes	Yes	No	Yes	No

Fig. 5 Nebulization speed and drop size distribution study as a function of applied frequency. (a) Droplet nebulization on the SAWN chip surface at the fundamental resonance frequency (Movie S2). (b) Table of the SAWN chip nebulization capability under different input frequencies with the same input power. (c) Average time to completely nebulize a 2 μL water droplet. Data is shown ± one standard deviation for n = 5. (d)-(f) Aerosolized drops diameter distribution plot under selected SAWN frequencies obtained by the aerodynamic particle sizer spectrometer. The bars demonstrate the aerosolized drop counts at each count median diameter (CMD) channel width. The measurement range was from 0.5 μm to 10 μm, limited by the detection instrument. A short inlet tube was selected and attached to the instrument to reduce the loss of aerosolized drops during the transport into the detection chamber and thus to improve the signal to noise ratio.

measurements 2 μL water droplets were pipetted on the same spot of the SAWN chip. For consistency in the nebulization process, we waited for 2 min between each measurement to let the chip return to ambient room temperature. As shown in Fig. 5 (c), different nebulization rates can be observed under different frequencies, which provided a tuning capability when a slower nebulization rate was required. We then characterized the size distribution of the tiny nebulized drops with an aerodynamic particle sizer spectrometer, shown in Fig. 5 (d)-(f). In general, the SAWN chip could nebulize the water droplet into a plume of extremely fine tiny drops. At 9.5603 MHz, finer drops were generated with a peak diameter at ~1.5 μm, while at both 23.1587 MHz and 26.9651 MHz, the aerosolized drops had similar peaks at ~3.5 μm. The nebulization size distribution was limited by the detection range of the particle sizer (0.5~10 μm) and the quantity of larger drop sizes could not be detected. Larger drops could have been captured by the inner sidewall of the inlet tube. Instrumentation with a wider detection range could be used in the future to improve the detection results. Instead of nebulizing the droplet by altering the nebulization frequency, the control over drop size distribution could be implemented by confining droplets in microcavities with different diameters and coupling the microcavity grids with the surface acoustic wave[56].

We then performed MS measurements with a standard test solution of Angiotensin II (m/z = 1046) in water with 0.1% formic acid. 1 μM and 100 nM of solutions were prepared. The experimental test setup is shown in Supplementary S3. Fig. 6 shows examples of MS results at different nebulization frequencies. (a1), (b1) and (c1) show the single Angiotensin II nebulized ion current trace as a function of time. For different input frequencies, the MS results showed different ion intensities within varied time length. For example, the nebulization detection ended abruptly at 9.5603 MHz but the

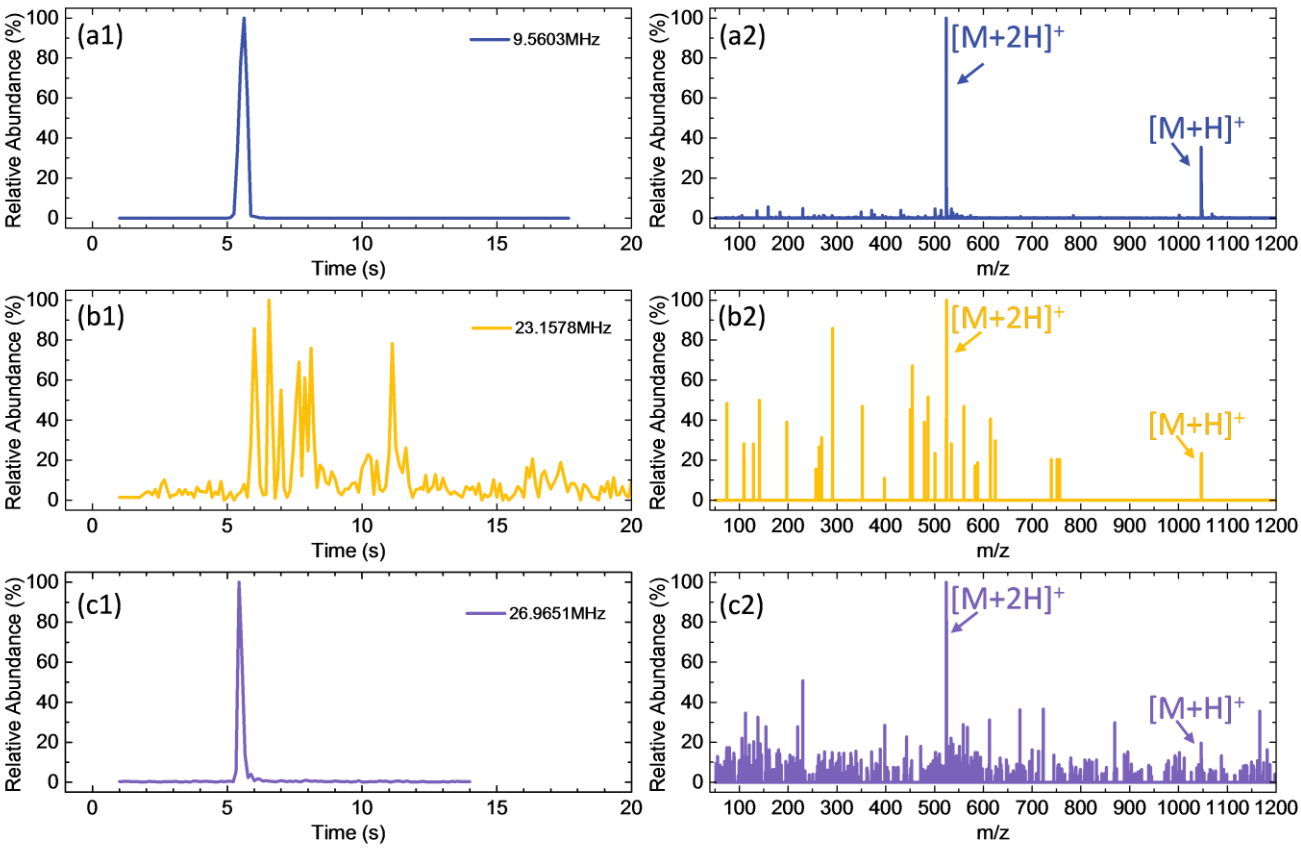

Fig. 6 Mass spectra at various frequencies. (a1), (b1) and (c1) show the Angiotensin II relative ion current versus time detected by the MS. The maximum ion current abundance counts were measured at $4.2x10^7$ for (a1), $1.0x10^3$ for (b1) and $3.0x10^5$ for (c1). (a2), (b2) and (c2) show the detailed Angiotensin II precursor ion mass spectra selected from the relative ion current. The highest relative ion abundance result was selected at the corresponding nebulization frequencies. A 2 μL water droplet was used for each measurement.

MS detection process lasted for tens of seconds at 23.1578 MHz, proving that the nebulization rate could be controlled by the nebulization frequencies. From (a2), (b2) and (c2), signature mass spectrums were generated successfully among all the frequencies with good signal to noise ratio. The SAWN generated the majority of $[M+2H]^{2+}$ ions, but $[M+H]^+$ ions were also detected. Depending on the nebulization frequencies, the intensity varied around 20%~35% compared with a base peak at $[M+2H]^{2+}$.

Conclusions

Here we present an integrated SAWN chip to perform droplet transport, merging, mixing and nebulization with ARCs and SW-SAWN. The innovations include: 1) we used only two AC signal inputs to generate the standing wave SAW and realized multiple lab-on-chip functions with the aid of ARC patterns. The system did not require complex control circuitry as compared to other technologies like EWOD; 2) the droplet could be manipulated on top of the SAWN chip in an open environment, without the need of an enclosed flow channel or top cover; 3) hydrophilic patterns were successfully created on the hydrophobic thin film with the aid of a Parylene C stencil mask to reposition and hold the water droplet; 4) nebulization was controlled at multiple resonance frequency nodes with the same IDE spacing design. We characterized the change of the droplet transport leading and trailing edge positions with time, self-resonance frequency transport speed and minimum power requirement, and we performed MS measurements at different nebulization frequencies. The results demonstrated that our ARC modified SAWN platform has great potential to serve as an integrated lab-on-chip platform for proteomics.

In the future we intend to explore the durability of the surface patterning and the influence of the top coating on the SAW amplitude as well as the power input. We will also perform tests with whole protein structures instead of peptides and integrate other protein-chemistry processes.

Conflicts of interest

D.R.G. has financial interests in Deurion LLC.

Acknowledgments

Fabrication was performed at the Washington Nanofabrication Facility (WNF), a member site of the NSF National Nanotechnology Coordinated Infrastructure (NNCI), with support from NSF award Nos. ECCS-1308025 and NNCI-

1542101. We would like to acknowledge the funding and fellowship support from CoMotion, the Clean Energy Institute at the University of Washington and the Amazon Catalyst Fund. We would like to thank Deurion LLC for the technical support with the power supply design and firmware upgrade. We would like to thank Jiayang He from the Novosselov Research Group for the technical support on the drop size measurements. D.R.G. thanks the National Institutes of Health for support (1R01AI123820-01) and the International Centre for Cancer Vaccine Science project of the International Research Agendas program of the Foundation for Polish Science co-financed by the European Union under the European Regional Development Fund (MAB/2017/03) at the University of Gdansk.

References

1. S. K. Cho, H. Moon and C.-J. Kim, *Journal of Microelectromechanical systems*, 2003, **12**, 70-80.
2. H. Geng, J. Feng, L. M. Stabryla and S. K. Cho, *Lab on a Chip*, 2017, **17**, 1060-1068.
3. P. Paik, V. K. Pamula and R. B. Fair, *Lab on a Chip*, 2003, **3**, 253-259.
4. D. Foresti, M. Nabavi, M. Klingauf, A. Ferrari and D. Poulikakos, *Proceedings of the National Academy of Sciences*, 2013, **110**, 12549-12554.
5. A. A. Darhuber, J. P. Valentino, S. M. Troian and S. Wagner, *Journal of Microelectromechanical Systems*, 2003, **12**, 873-879.
6. J. Brzoska, F. Brochard-Wyart and F. Rondelez, *Langmuir*, 1993, **9**, 2220-2224.
7. H. Linke, B. Alemán, L. Melling, M. Taormina, M. Francis, C. Dow-Hygelund, V. Narayanan, R. Taylor and A. Stout, *Physical review letters*, 2006, **96**, 154502.
8. C. N. Baroud, M. R. de Saint Vincent and J.-P. Delville, *Lab on a Chip*, 2007, **7**, 1029-1033.
9. P.-Y. Chiou, Z. Chang and M. C. Wu, *Journal of Microelectromechanical Systems*, 2008, **17**, 133-138.
10. K. S. Khalil, S. R. Mahmoudi, N. Abu-Dheir and K. K. Varanasi, *Applied physics letters*, 2014, **105**, 041604.
11. T. A. Duncombe, E. Y. Erdem, A. Shastry, R. Baskaran and K. F. Böhringer, *Advanced materials*, 2012, **24**, 1545-1550.
12. T. A. Duncombe, J. F. Parsons and K. F. Böhringer, *Langmuir*, 2012, **28**, 13765-13770.
13. D. Chatterjee, B. Hetayothin, A. R. Wheeler, D. J. King and R. L. Garrell, *Lab on a Chip*, 2006, **6**, 199-206.
14. M. Abdelgawad, S. L. Freire, H. Yang and A. R. Wheeler, *Lab on a Chip*, 2008, **8**, 672-677.
15. A. Takei, K. Matsumoto and I. Shomoyama, *Lab on a Chip*, 2010, **10**, 1781-1786.
16. T. Jones, *Journal of Electrostatics*, 2001, **51**, 290-299.
17. J. Shi, D. Ahmed, X. Mao, S.-C. S. Lin, A. Lawit and T. J. Huang, *Lab on a Chip*, 2009, **9**, 2890-2895.
18. Z. Takats, J. M. Wiseman, B. Gologan and R. G. Cooks, *Science*, 2004, **306**, 471-473.
19. Y. Li, X. Wang and R. K. Ernst, *Rapid Communications in Mass Spectrometry*, 2011, **25**, 2641-2648.
20. S. A. Shaffer, M. D. Harvey, D. R. Goodlett and R. K. Ernst, *Journal of the American Society for Mass Spectrometry*, 2007, **18**, 1080-1092.
21. E. C. Yi, H. Lee, R. Aebersold and D. R. Goodlett, *Rapid communications in mass spectrometry*, 2003, **17**, 2093-2098.
22. H. Moon, A. R. Wheeler, R. L. Garrell and J. A. Loo, *Lab on a Chip*, 2006, **6**, 1213-1219.
23. O. Kudina, B. Eral and F. Mugele, *Analytical chemistry*, 2016, **88**, 4669-4675.
24. T. Nara, M. Takasaki, T. Maeda, T. Higuchi, S. Ando and S. Tachi, *IEEE Computer Graphics and Applications*, 2001, **21**, 56-63.
25. M. Takasaki, T. Nara, S. Tachi and T. Higuchi, 2000.
26. D. P. Morgan, *Surface-wave devices for signal processing*, Elsevier Amsterdam, 1985.
27. P. Sharma and K. Sreenivas, *Applied physics letters*, 2003, **83**, 3617-3619.
28. R. J. Shilton, V. Mattoli, M. Travagliati, M. Agostini, A. Desii, F. Beltram and M. Cecchini, *Advanced Functional Materials*, 2015, **25**, 5895-5901.
29. T. Franke, A. R. Abate, D. A. Weitz and A. Wixforth, *Lab on a Chip*, 2009, **9**, 2625-2627.
30. J. H. Jung, G. Destgeer, B. Ha, J. Park and H. J. Sung, *Lab on a Chip*, 2016, **16**, 3235-3243.
31. K. M. Kabir, Y. M. Sabri, G. I. Matthews, L. A. Jones, S. J. Ippolito and S. K. Bhargava, *Analyst*, 2015, **140**, 5508-5517.
32. S. A. Tadesse and M. Li, *Nature communications*, 2014, **5**, 5402.
33. D. Munk, M. Katzman, M. Hen, M. Priel, M. Feldberg, T. Sharabani, S. Levy, A. Bergman and A. Zadok, *Nature communications*, 2019, **10**, 1-9.
34. M. Kurosawa, T. Watanabe, A. Futami and T. Higuchi, *Sensors and Actuators-A-Physical Sensors*, 1995, **50**, 69-74.
35. Y. Huang, S. R. Heron, A. M. Clark, J. S. Edgar, S. H. Yoon, D. P. A. Kilgour, F. Turecek, A. Aliseda and D. R. Goodlett, *Journal of Mass Spectrometry*, 2016, **51**, 424-429.
36. L. Pintabona, A. Astefanei, G. L. Corthals and A. C. van Asten, *Journal of The American Society for Mass Spectrometry*, 2019, **30**, 2655-2669.
37. S. R. Heron, R. Wilson, S. A. Shaffer, D. R. Goodlett and J. M. Cooper, *Analytical Chemistry*, 2010, **82**, 3985-3989.
38. J. Ho, M. K. Tan, D. B. Go, L. Y. Yeo, J. R. Friend and H.-C. Chang, *Analytical chemistry*, 2011, **83**, 3260-3266.
39. Y. Bourquin, R. Wilson, Y. Zhang, J. Reboud and J. M. Cooper, *Advanced materials*, 2011, **23**, 1458-1462.
40. J. Reboud, R. Wilson, Y. Zhang, M. H. Ismail, Y. Bourquin and J. M. Cooper, *Lab on a Chip*, 2012, **12**, 1268-1273.
41. T. A. Duncombe, J. F. Parsons and K. F. Böhringer, *Langmuir*, 2012, **28**, 13765-13770.
42. D. Sun and K. F. Bohringer, *Micromachines (Basel)*, 2019, **10**, 101.
43. D. Sun and K. F. Böhringer, *Journal of Physics: Conference Series*, 2018, **1052**, 012014.
44. L. Monkkonen, J. S. Edgar, D. Winters, S. R. Heron, C. L. Mackay, C. D. Masselon, A. A. Stokes, P. R. Langridge-Smith and D. R. Goodlett, *Journal of Chromatography A*, 2016, **1439**, 161-166.
45. J. Ju, Y. Yamagata, H. Ohmori and T. Higuchi, *Sensors and Actuators A: Physical*, 2008, **147**, 570-575.

46. S. H. Yoon, T. Liang, T. Schneider, B. L. Oyler, C. E. Chandler, R. K. Ernst, G. S. Yen, Y. Huang, E. Nilsson and D. R. Goodlett, *Rapid Communications in Mass Spectrometry*, 2016, **30**, 2555-2560.
47. D. Beyssen, L. Le Brizoual, O. Elmazria and P. Alnot, *Sensors and Actuators B: Chemical*, 2006, **118**, 380-385.
48. D. Sun and K. F. Böhringer, *Applied Physics Letters*, 2020, **116**, 093702.
49. J. Ju, Y. Yamagata, H. Ohmori and T. Higuchi, *Sensor Actuat a-Phys*, 2008, **147**, 570-575.
50. X. Noblin, A. Buguin and F. Brochard-Wyart, *The European Physical Journal E*, 2004, **14**, 395-404.
51. P. Brunet, M. Baudoin, O. B. Matar and F. Zoueshtiagh, *Physical Review E*, 2010, **81**, 036315.
52. Y. Dong, H. R. Holmes and K. F. Böhringer, *Langmuir*, 2017, **33**, 10745-10752.
53. H. R. Holmes and K. F. Böhringer, *Advances in Colloid and Interface Science*, 2018, **255**, 18-25.
54. A. Qi, L. Y. Yeo and J. R. Friend, *Physics of Fluids*, 2008, **20**, 074103.
55. S. Kooij, A. Astefanei, G. L. Corthals and D. Bonn, *Scientific reports*, 2019, **9**, 1-8.
56. E. Nazarzadeh, R. Wilson, X. King, J. Reboud, M. Tassieri and J. M. Cooper, *Physics of Fluids*, 2017, **29**, 112105.